

Article

Evaluation of Engineering Site and Subsurface Structures Using Seismic Refraction Tomography: A Case Study of Abydos Site, Sohag Governorate, Egypt

Abdelbaset M. Abudeif ^{1,*}, Gamal Z. Abdel Aal ², Nessreen F. Abdelbaky ^{3,4}, Ahmed M. Abdel Gowad ⁵ and Mohammed A. Mohammed ¹

¹ Geology Department, Faculty of Science, Sohag University, Sohag 82511, Egypt

² Geology Department, Faculty of Science, Assiut University, Assiut 71515, Egypt

³ Geophysics Exploration, Dessert Research Center, Al Mataria, Cairo 4540064, Egypt

⁴ Biology Department Yanbu Branch, Taibah University, Al Madina Al Munawwarah 46424, Saudi Arabia

⁵ Geology Department, Faculty of Science, South Valley University, Qena 83523, Egypt

* Correspondence: a.abudeif@science.sohag.edu.eg

Abstract: Because of the strategic importance of the Abydos archaeological site in Egypt as a source of wealth for Egyptian tourism, this study was concerned with carrying out geophysical measurements to detect subsurface succession and measure variations in the geotechnical engineering features of the soils/rocks in order to protect this significant area. The findings will assist geologists and seismologists in collaborating with archaeologists for future site development, revitalization, and investment. The primary objectives of this work were to determine the subsurface lithology, evaluate the engineering geotechnical properties of soils/rocks, identify the layer thicknesses, and identify the site class by calculating V_s^{30} . To achieve these goals, seventeen (17) seismic refraction tomography (SRT) P- and S-wave measurements were executed in front of the Osirion location. SeisImager Software was used for the processing and interpretation of the outcomes. The results were the travel time–distance curves, which were used for building the 2D seismic models that exhibited the velocity and the depth of the layered models. These models were validated by our previous works using electric resistivity tomography and borehole data. The results indicated that this site consisted of three geoseismic subsurface layers. The first layer was the surface that was made up of wadi deposits, which were a mixture of gravel, sand, and silt and were characterized by incompetent to slightly competent materials. The second layer corresponded to the sand and muddy sand deposits of competent rock that was of fair to moderate quality. The third layer (clay deposits) had a higher velocity and was more compact and may be employed as a bedrock layer. The elastic moduli, V_s^{30} , petrophysical, and geotechnical properties of the three geoseismic layers were appraised as essential parameters. Integration of petrophysical and geotechnical parameters and elastic moduli revealed that the third layer was composed of competent clays, which were characterized by low values of porosity, void ratio, Poisson ratio, and stress ratio. It also had a high rigidity, Young's and bulk moduli, concentration and material indexes, N-value, ultimate bearing capacities, and high density values, and vice versa for the first layer. The standard NEHRP site class was B (rocks). These parameters are ordinarily used as key indications and serve as significant inputs for any future work.

Keywords: seismic refraction tomography; archaeological site; site evaluation; elastic moduli; V_s^{30} ; NEHRP site class



Citation: Abudeif, A.M.; Abdel Aal, G.Z.; Abdelbaky, N.F.; Abdel Gowad, A.M.; Mohammed, M.A. Evaluation of Engineering Site and Subsurface Structures Using Seismic Refraction Tomography: A Case Study of Abydos Site, Sohag Governorate, Egypt. *Appl. Sci.* **2023**, *13*, 2745. <https://doi.org/10.3390/app13042745>

Academic Editor: Roberto Zivieri

Received: 3 January 2023

Revised: 2 February 2023

Accepted: 16 February 2023

Published: 20 February 2023



Copyright: © 2023 by the authors. Licensee MDPI, Basel, Switzerland. This article is an open access article distributed under the terms and conditions of the Creative Commons Attribution (CC BY) license (<https://creativecommons.org/licenses/by/4.0/>).

1. Introduction

The Abydos archaeological site serves as the most prestigious burial place for kings and top court officials in ancient Egypt due to its strategic location, great tourism value, and importance. This study investigated the engineering importance of this site from a

strategic standpoint, as it is an archaeological site with explored archaeological features and unexplored archaeological ones where new facilities are likely to be established.

The main objectives of this work were (1) to determine the subsurface lithology of the subsurface succession, (2) to determine the geotechnical properties of the rocks/soils and their degree of competence for the stability of buildings in this site, and (3) to determine the petrophysical characteristics of the rocks/soils in this important archaeological site.

Geophysical approaches as near-surface investigations are used in a wide range of fields, including archaeology [1], geotechnical engineering [2,3], and civil engineering [4,5]. One of the vital approaches for complicated structures and geologic sequences investigation near the surface is seismic refraction tomography. This technique has a wide variety of applications in the field of engineering [6]. According to the National Earthquake Hazard Reduction Program's criteria, the main shallow subsurface feature for the determination of seismic site classes is called V_s^{30} [7]. The relevance of V_s^{30} is attributed to the site amplification sensitivity by the shear wave velocity at the near surface and ground motion intensity [8,9].

The ancient site of Abydos is situated in Sohag Governorate, about 13 km west of El-Balyana city (Figure 1), between latitudes $26^{\circ}10' N$ and $26^{\circ}15' N$, and longitudes $31^{\circ}53' E$ and $31^{\circ}57' E$. The study area is situated west of the Osirion site behind the Abydos temple. The studied site was flat, and thus, no topographic corrections for acquiring data were needed.

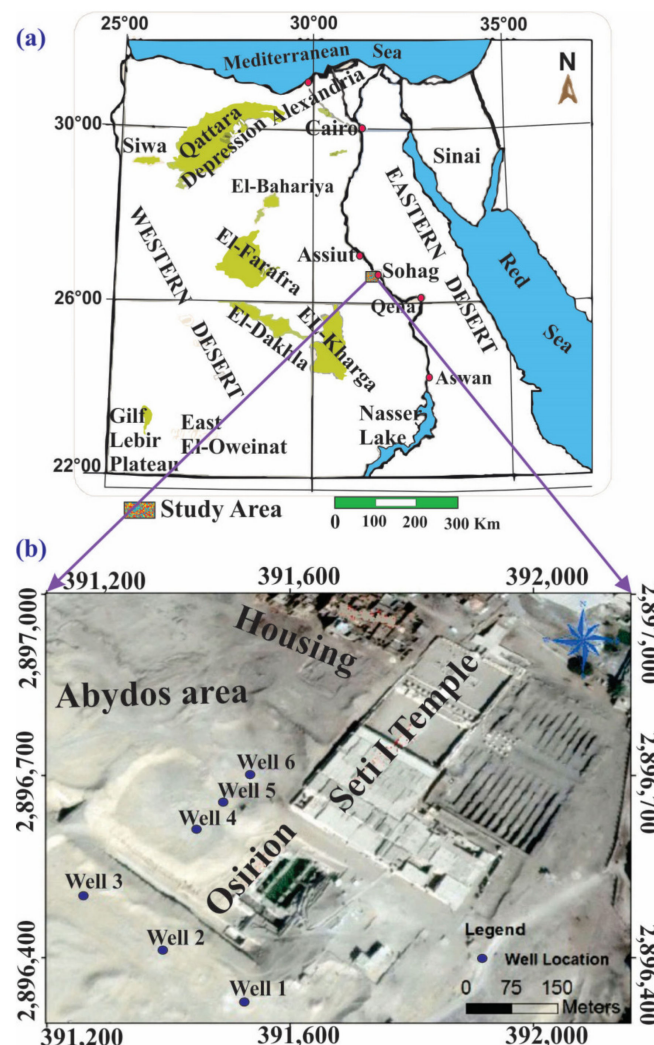


Figure 1. Location map for the Abydos site, with (a) a map of Egypt and (b) a more comprehensive map of the Abydos temple that depicts the Osirion site and nearby boreholes.

2. Historical Background

The Abydos site is considered one of the most touristy places in ancient Egypt. Numerous historic temples, the royal necropolis, and Umm El-Qa'ab, where the first pharaohs were buried, were all located in the ancient land of Abydos. The oldest dynasties selected it as a burial site, while subsequent rulers, such as Ramses II and Seti I, constructed temples and shrines [1]. Abydos Temple was built on two successive sections, one of which was supported by Holocene Nile deposits and the other by older Nile deposits that were created from the Nile terrace. The Osirion, which was built 15 m below the surface of the ground below the Temple of Seti I, was where the Pharaonic death rite took place. Abydos reached the height of its splendor during the reigns of these two monarchs. For both religious and political reasons, Seti I built a temple there for himself and his father Ramses I [1]. It is expected that new activities, such as constructions or explorations, may be undertaken at this site.

3. Geological Setting

The study area is a part of the Nile Valley, which was geologically studied by other authors [10–12]. Geologically, the whole of the Abydos site is associated with a large stretch of Quaternary to Pliocene deposits that uncomfortably overlay the Esna Shale, which is Early Tertiary in age [12]. Figure 2 shows the geology of Sohag province, including the study area. Various rock units that are distinguished in the Abydos site are composed mainly of sedimentary deposits and are arranged in the following order from older to younger: (i) Pliocene clays, (ii) Qena sands, (iii) Kom Ombo gravels, (iv) Ghawanim Formation, and (v) Dandara Formation, which range from the Pliocene to recent [13]. The main formation that contains groundwater in the study area is known as the Qena Sands Formation. It is scarcer in the west direction, where it cuts a Lower Eocene limestone plateau. Some of these sands were eroded by the River Nile and its valley to the east, and as a result, the current Nile and its plain are filled with silts. Results from three wells nearby Abydos Temple (well numbers 1, 2, and 3) indicate that part of the Qena sands is sometimes 15 m thick [14]. According to Said [15], the basal deposits above the Lower Eocene limestone are distinguished by a variety of clay deposits with scattered silt intercalation. These clays are compared with Paleonile deposits.

Said [15] categorized the investigated site into three main components from a geomorphological perspective: the structural limestone plateau, the Nile terraces, and the Nile floodplain. The limestone plateau is characterized by high relief that often reaches 200–375 m and borders the Nile Valley from both directions. It is divided by several NE–SW and ENE–WSW trending crosswise dry wadis, some of which are currently filled with sands and gravels. A general slope toward the Nile Valley is attained through these wadis [16]. The Nile Terraces are situated between the agricultural plains and the limestone plateau's margins on both sides of the Nile Valley. It has a surface made of sands and gravels. Most of these desert fringes are represented by a sequence of subsequent terraces at intermediate altitudes (70–140 m) above the main sea level. These terraces are remnants of the previous alluvial plains [17]. The fertilized shale, silt, and mud utilized for agriculture make up the Nile flood plain, which includes the farmed area on both sides of the River Nile. With an elevation ranging from 55 to 65 m above the sea level in the Sohag district, the floodplain is virtually flat or gradually slopes down northward. In comparison to the eastern side of the Nile Valley, the cultivated areas are much wider on the western side.

The Nile Valley was structurally bordered by the limestone plateau, which also created high relief structures with heights of 200–375 m. It is divided by several crossing dry wadis that trend NE–SW and ENE–WSW, some of which are currently filled with sands and gravels. These wadis eventually slope downward toward the Nile Valley. Most of these wadis have undergone several cycles of activity, separated by active (arid) ones, and are structurally restricted [16].

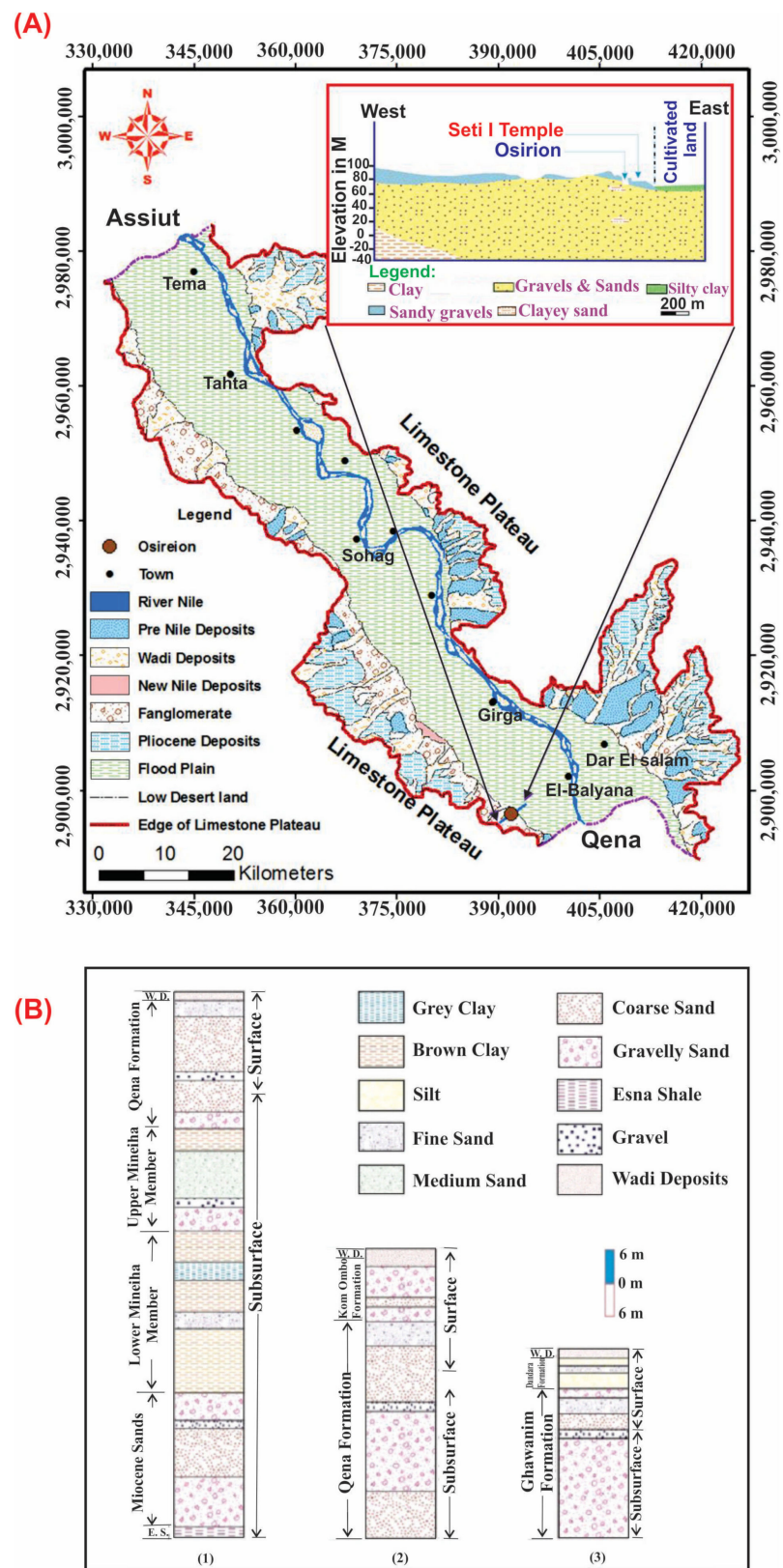


Figure 2. (A) A geological map of the Sohag district, including the investigated area, emphasizing the major surface geologic units and a cross-section through the study site passing by the Osirion location [14]. (B) From the three drilled wells (1, 2, and 3) that were situated in the research site, the stratigraphic sequence west of the Abydos area was determined [18].

4. Material and Methods

4.1. Shallow Seismic Refraction Method

The shallow seismic refraction technique was used to investigate unknown subsurface areas in detail. This technique is based on Snell's law, which regulates how waves that are propagating over layers of differing seismic wave velocities are refracted. Once those waves' arrival times are measured at the surface, they can be inverted to determine the characteristics of the rock they traveled through [19–21]. Rock velocities, depths, and thicknesses are the main outputs of this technique. The seismic refraction tomography approach for site investigation is more powerful when it is compared with traditional electrical resistivity tomography [22]. Seismic waves produced by man-made sources, such as sledgehammers, travel across a medium in the seismic refraction method and are bent at interfaces where the density (acoustic impedance) or the seismic velocity varies. Waves returning to the surface after traversing various depths in the subsurface are recorded by different geophones arranged in a straight line. The seismic velocity in the subsurface and the depth of the interfaces are determined by measuring the amount of time that passes between the break and the recording of a seismic signal. Simple assumptions about the velocity structure are made in conventional analyses of seismic refraction data sets; however, these assumptions are at variance with the lateral discontinuities, observed heterogeneity, and gradients [23].

P-wave refraction demonstrated its effectiveness in determining the depth to the bedrock within the framework of site assessment research [24–26]. However, horizontal shear (SH) wave refraction is employed to investigate subsurface layers only to certain depths and in the right circumstances [27]. Combining P- and S-wave refraction techniques improves our knowledge of subsurface geology or provides supplemental data. Because changes in saturation, elastic moduli, or porosity impact P- and S-waves differently, they are crucial for differentiating various lithological compositions [28,29]. In order to provide subsurface volumetric imaging of lithologic and geotechnical variables, P- and S-wave seismic refraction tomography is a powerful tool. Recent studies demonstrated that seismic refraction tomography, which uses both P- and S-waves, is used to systematically evaluate V_s^{30} and geotechnical variables that are more sensitive to variations in the subsurface soil characteristics [30,31]. Additionally, V_s^{30} is used to establish the NEHRP site class of a location [32].

4.2. Data Acquisition

P- and S-wave refraction data were collected along 17 acquisition lines in front of the Osirion site, forming a consistent grid, where 9 lines were oriented NW–SE and 8 lines were oriented perpendicular to them (Figure 3). The total length of each line was 200 m, and each was composed of two overlapped spreads. The length of each spread was 115 m, with an overlapping distance of 30 m. The total number of geophones in each line was 41 geophones, with an interval of 5 m. To acquire the P-wave and S-wave data, 14 Hz vertical and horizontal geophones were used, respectively. Five shots were employed for each spread at distances of −2.5, 27.5, 57.5, 87.5, and 117.5 m. A sledgehammer with a mass of 15 kg was used as a seismic source. For the P-wave refraction, the sledgehammer was struck vertically on a steel plate, while it was struck horizontally on a wooden truck for the S-wave refraction data [33]. For both acquisitions, the shots were stacked 3 to 5 times. The shots were recorded on a 24-channel Geometrics® GEODE, with a 0.25 ms sampling interval and a recording length of 200 ms. No acquisition filters were applied.

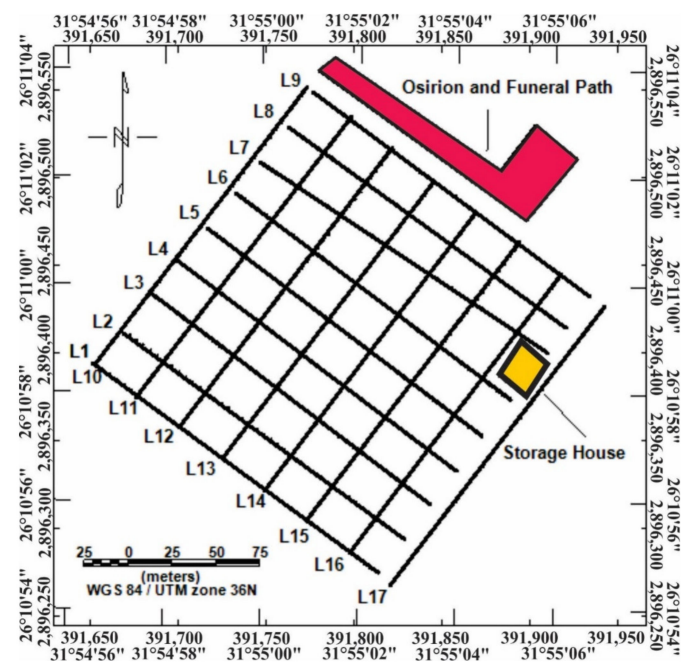


Figure 3. The configuration of the seismic refraction lines for P- and S-waves in the current investigation.

4.3. Data Processing

The obtained seismic refraction data were processed and interpreted using the SeisImager/2D[®] software (Plotrefa v.3.0.0.6, 2014, and Pickwin v.5.1.1.2, 2014) offered by Geometrics. Shot records provided the geometry, including the shots and the geophone positions and altitudes, for all the acquired seismic data [34]. After visual verification with Pickwin, the first arrival times were manually selected for both the P- and S-wave shot records. Figure 4 illustrates the first-break picking for the P- and S-waves on Pickwin's line no. 1.

Plotrefa software was used to produce the travel time–distance curves by plotting the first arrival times for all the shots along every surveyed line versus the source-to-geophone distances. In Plotrefa, these curves were displayed, examined, and some of them were modified for more precise data explanation. The research site suffered lateral velocity variation because of the lateral lithologic, fluid content, and geotechnical variations in the subsurface. Therefore, the interpretation of this work employed seismic refraction tomographic inversion. A refraction seismic survey's ultimate goal is to derive seismic velocity–depth sections that detail the depths and thicknesses of each layer and their respective velocities. The initial model was created using data from prior studies, including previous geological and geophysical data, field outcrops and exposures, accessible borehole data, and modeling outcomes from previous works of the same authors of electric resistivity tomography and borehole data in the researched area [35].

The inversion for both P- and S-wave data was carried out using the same software (Plotrefa), which employs nonlinear travel time tomography [36,37], consisting of ray tracing for forward modeling and a simultaneous iterative reconstruction technique (SIRT) for inversion. The default inversion parameters for this software are 10 iterations, 3 nodes, and a smoothing weight of 0.5. There are no limitations on the number of layers or their thicknesses in the Plotrefa package's inversion method. As a result, these parameters are not constant in the models. The initial model was created mostly using the ERT section from the prior investigation of the same study region [35]. The minimum and maximum velocities used in the initial models were calculated using another software package that inverted the data based on the homogeneous function method [38]. The authors utilized an initial model with 15 layers (the program's default setting). The used velocities were those that gave the lowest RMSE.

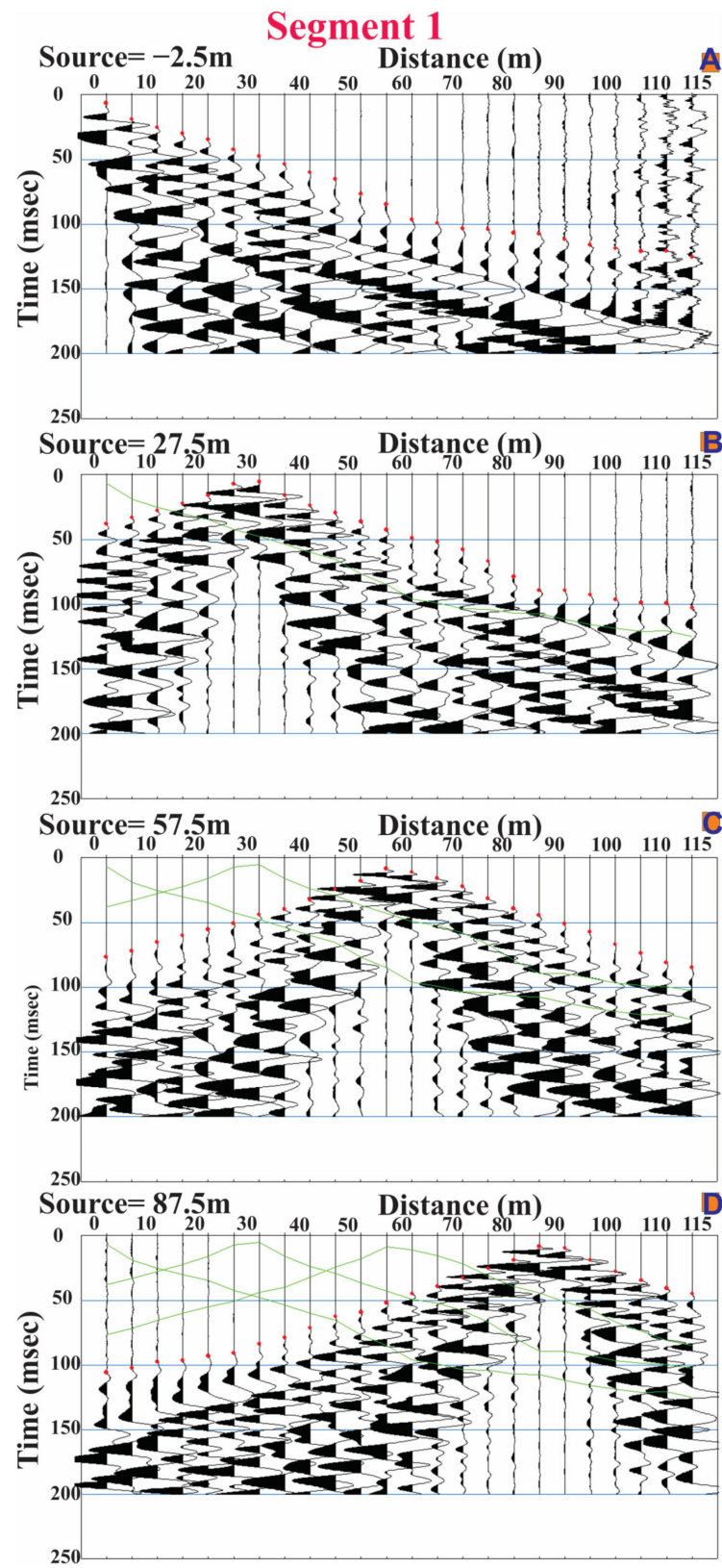


Figure 4. Cont.

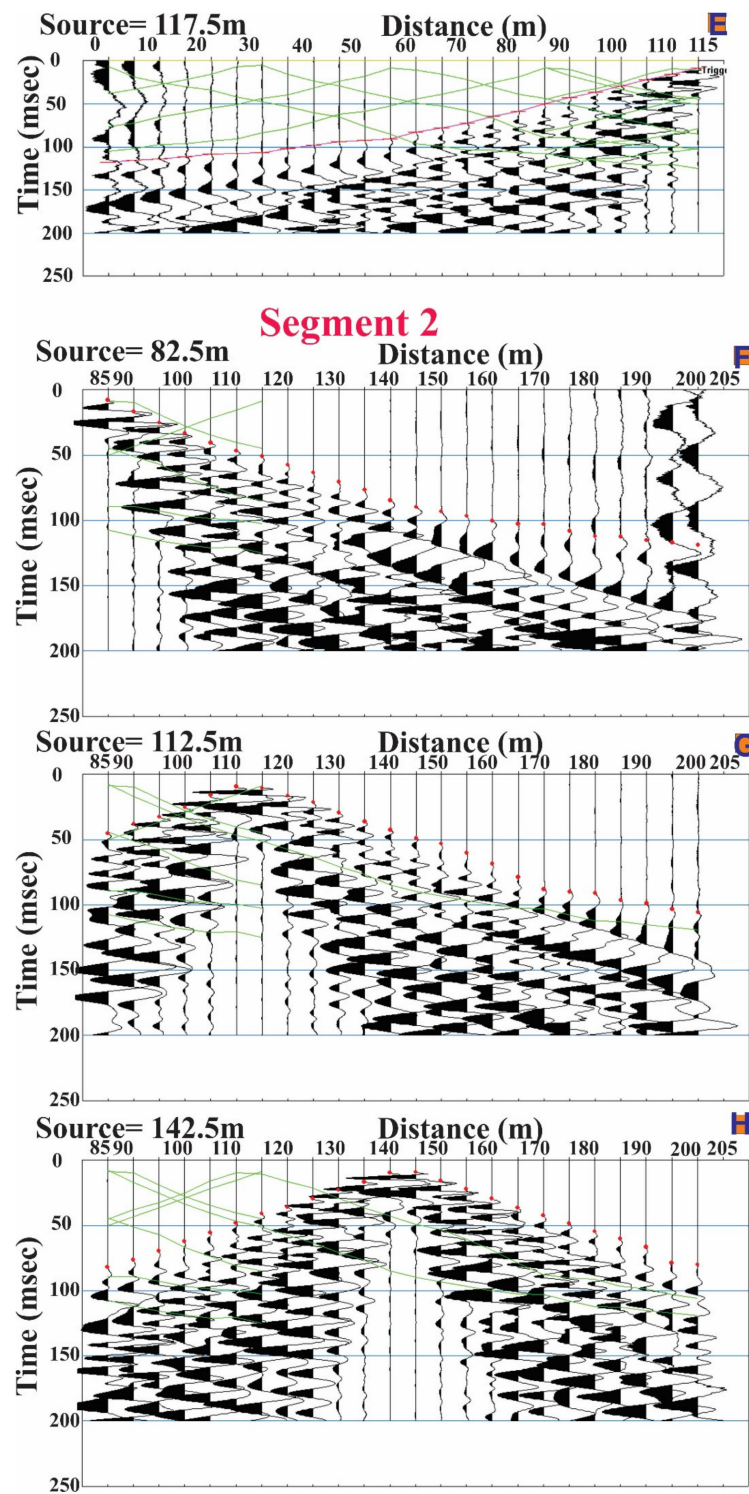


Figure 4. Cont.

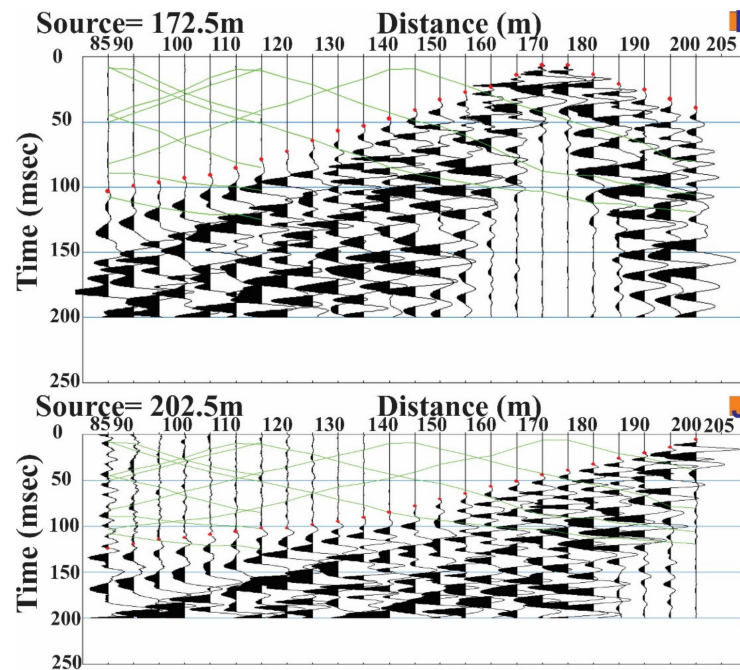


Figure 4. Examples of the obtained picked refraction seismic data for profile 1, which involved two segments. In segment 1, there was (A) a P-wave shooting forward at a distance of -2.5 m, (B) a P-wave shooting at the mid-point between geophones 6 and 7 at a distance of 27.5 m, (C) a P-wave shooting at the mid-point of the profile at a distance of 57.5 m, (D) a P-wave shooting at the mid-point between geophones 18 and 19 at a distance of 87.5 m, and (E) a P-wave shooting at a distance of 117.5 m. In segment 2, there was (F) a P-wave shooting forward at a distance of 82.5 m, (G) a P-wave shooting at a distance of 112.5 m, (H) a P-wave shooting at a distance of 142.5 m, (I) a P-wave shooting at a distance of 172.5 m, and (J) a P-wave shooting at a distance of 202.5 m.

A velocity model without small-scale aberrations was produced by iteratively modifying the resulting model to decrease the RMS error between the estimated and actual travel times. The raytracing application from Plotrefa was used to evaluate the models. An important consideration when assessing a seismic refraction interpretation is the model–data compatibility. This is done by comparing the differences between the synthetic data produced by models and the first arrival data in the field [39]. Using this raytracing, the theoretical travel times were computed and presented along with the observed data and the RMS error. The RMS error between the calculated and observed values was less than 4 ms, indicating the best fit between the observed and estimated travel times, as shown in Figure 5.

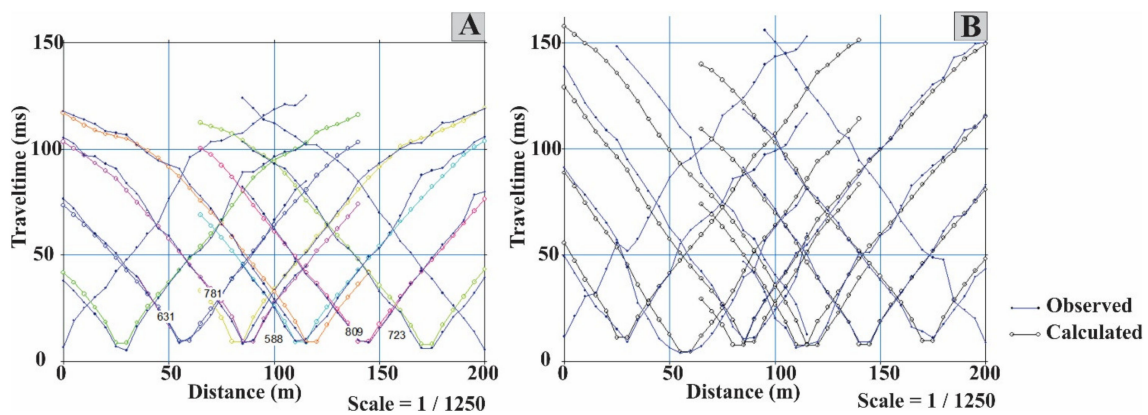


Figure 5. The observed and calculated travel time–distance curves of the seismic refraction profile 1 (A) for the P-wave and (B) for the S-wave.

5. Results and Discussion

Figures 6–9 display the final depth–velocity models produced from the seismic refraction tomography for the seventeen lines. These models demonstrated that the studied site was constituted primarily of three geoseismic subsurface layers based on the seismic inversion and the calibration with the pre-implemented geo-electric resistivity studies in this site [35]. Figure 10 illustrates an example of a two-dimensional ERT profile that included a well location.

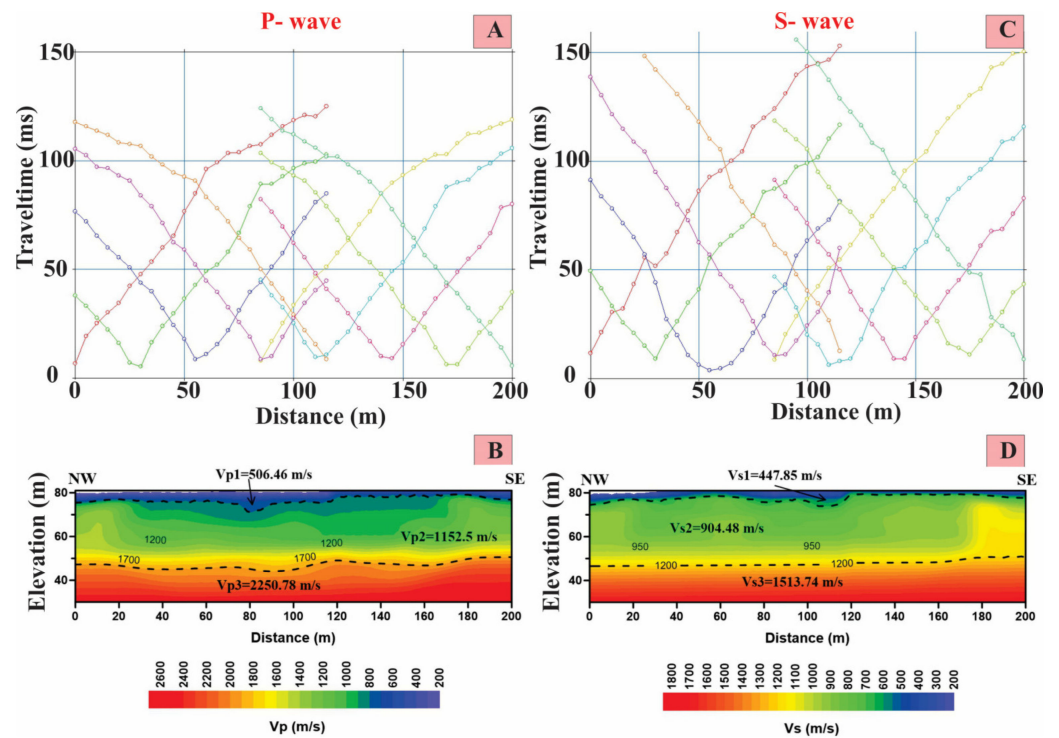


Figure 6. Example of the seismic refraction profile 1: (A) travel time–distance curve derived from the P-wave profile; (B) 2D depth–velocity model derived from P-wave profile; (C) travel time–distance curve derived from the S-wave profile; and (D) 2D depth–velocity model derived from the S-wave profile.

These findings were consistent with the results of nearby boreholes scattered near the study site. A careful examination of both the P- and S-wave velocities 2D seismic models revealed that the maximum derived depth was 50 m. The range of the P- and S-wave velocities for the derived shallow subsurface geoseismic layers were 356.38 m/s to 2821.81 m/s and 225.83 m/s to 1896.28 m/s, respectively.

The V_p and V_s values of the first geoseismic surface layer changed from 356.38 to 618.2 m/s and 225.83 to 496.24 m/s, respectively. It was composed of wadi deposits, which were made up of gravel, sand, and silt, and its thickness varied between 1.5 and 4.8 m. The V_p and V_s values of the second geoseismic layer varied from 1064.44 to 1303.6 m/s and 833.24 to 1119.74 m/s, respectively. Its lithology showed intercalated sand and muddy sand deposits. The thicknesses of this layer ranged from 14.7 to 35 m. The V_p and V_s values of the third geoseismic layer varied from 1955 m/s to 2821.81 m/s and 1155 to 1896.28 m/s, respectively. Its lithological nature was clay deposits, with its thickness undefined. All 17 velocity–depth models are shown in Figures 6–9. The results of the 17 surveyed profiles are summarized in Table 1. A careful investigation of the previous models indicated that there was no fracturing or faulting in front of the Osirion site according to the interpretation of the seismic wave velocities and the final geoseismic models.

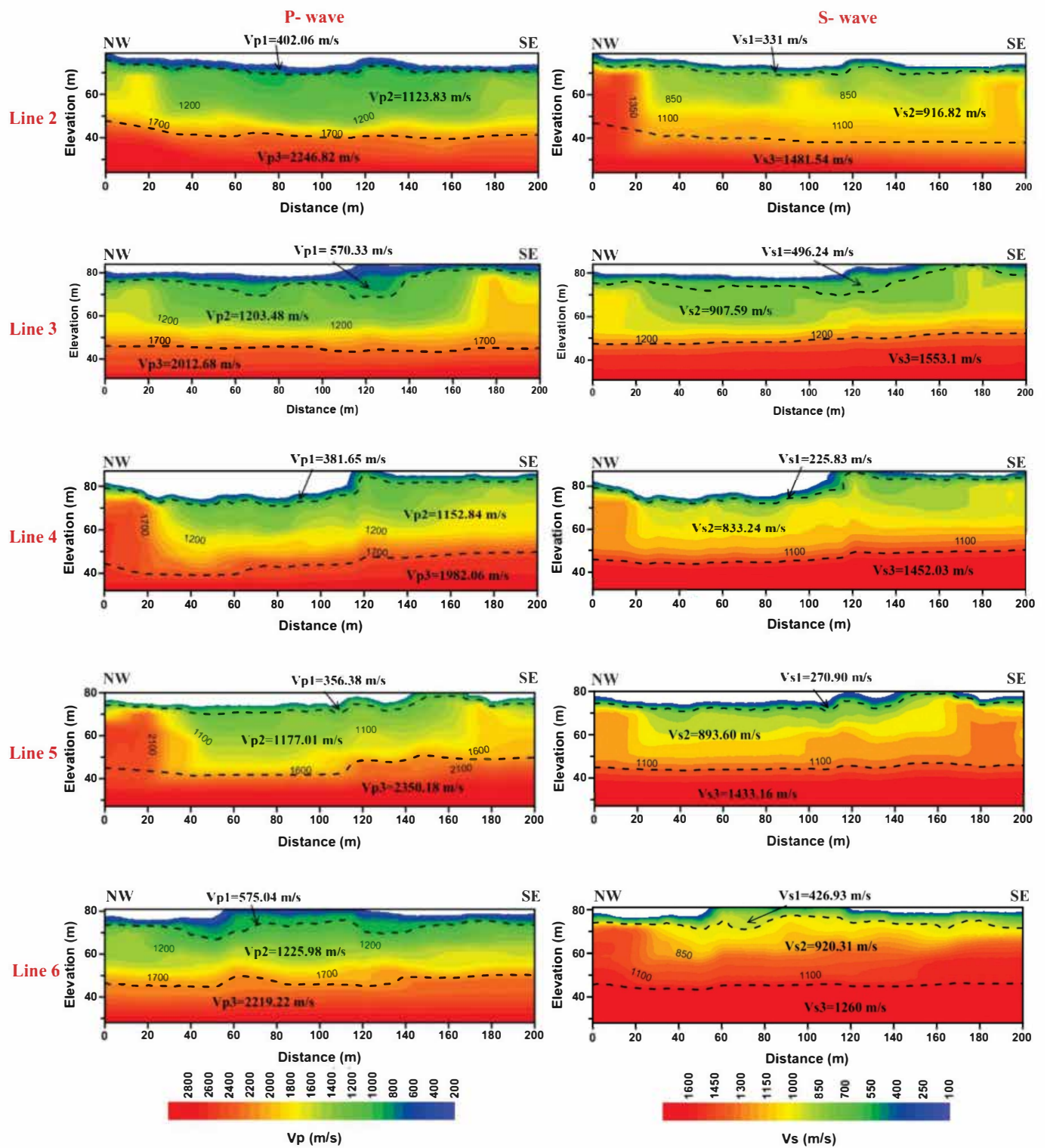


Figure 7. The 2D depth-velocity models for the P-wave and associated S-wave profiles along the NW-SE direction were produced.

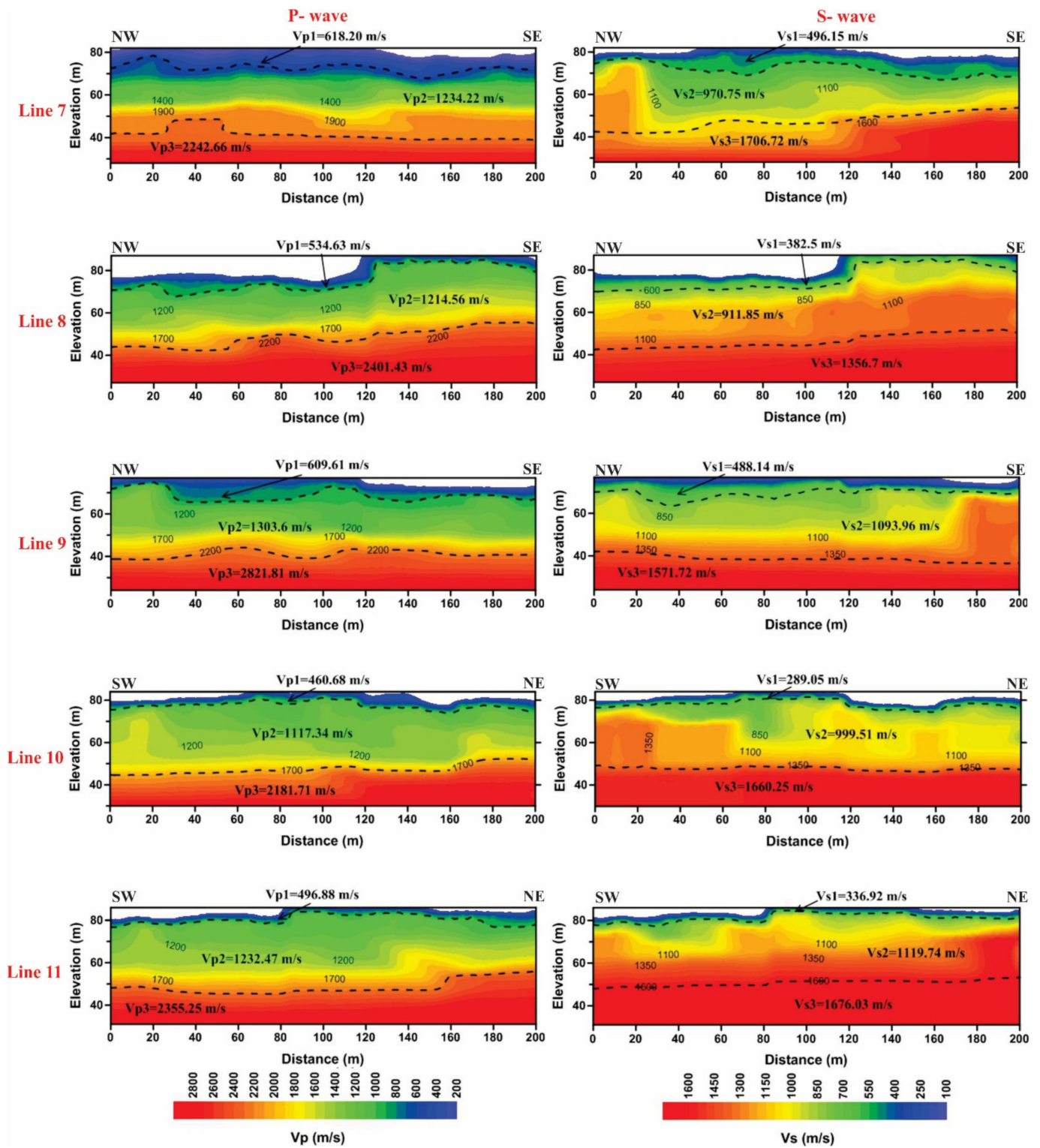


Figure 8. The 2D depth-velocity models for the P-wave and associated S-wave profiles along the NW-SE and SW-NE directions were produced.

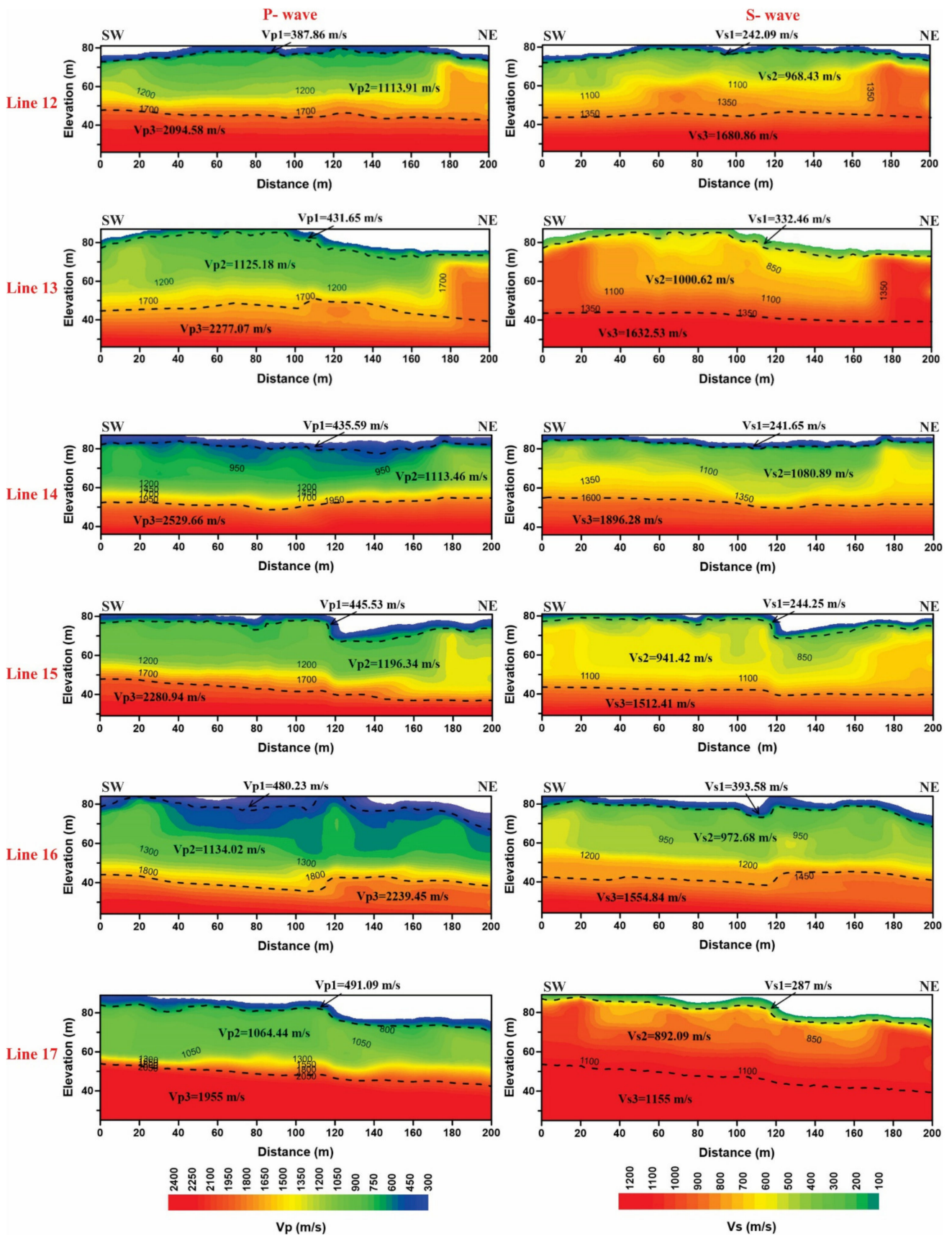


Figure 9. The 2D depth-velocity models for the P-wave and associated S-wave profiles along the NW-SE and SW-NE directions were produced.

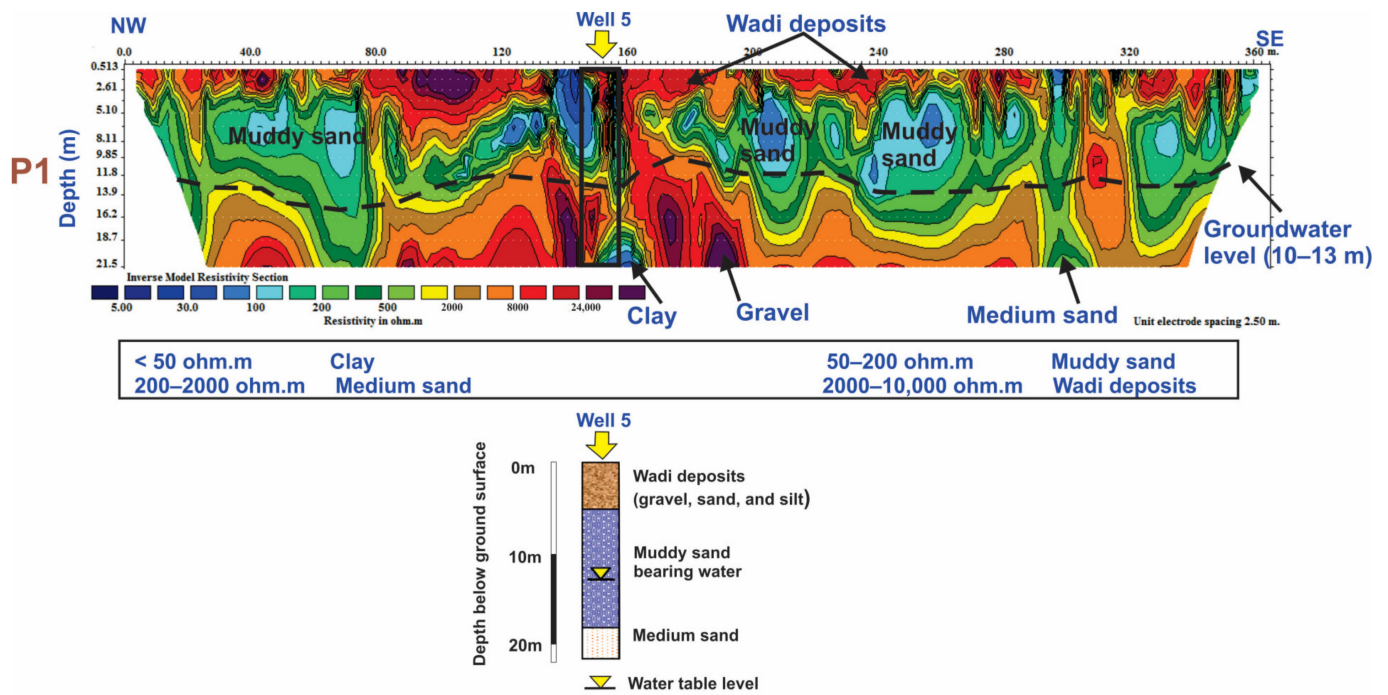


Figure 10. The 2D electrical resistivity model of profile 1. This model emphasized the distinctive geoelectric zones that were identified using the borehole and resistivity data that were available and it also showed the depth of the groundwater level.

Table 1. V_p and V_s values for the first, second, and third layers, as well as the depth to the top of the second and third layers, for each of the 17 seismic refraction profiles.

Profile No.	First Layer		Second Layer		Third Layer		Depth to the Top of	
	V_p (m/s)	V_s (m/s)	V_p (m/s)	V_s (m/s)	V_p (m/s)	V_s (m/s)	Second Layer	Third Layer
1	506.46	447.85	1152.5	904.48	2250.78	1513.74	−3.6	−18.7
2	402.06	331	1123.83	916.82	2246.82	1481.54	−1.5	−19.5
3	570.33	496.24	1203.48	907.59	2012.68	1553.1	−4.8	−18.9
4	381.65	225.83	1152.84	833.24	1982.06	1452.03	−1.5	−14.7
5	356.38	270.9	1177.01	893.6	2350.18	1433.16	−1.8	−18.1
6	575.04	426.93	1225.98	920.31	2219.22	1260	−3.1	−19.7
7	618.2	496.15	1234.22	970.75	2242.66	1706.72	−4.8	−23.0
8	534.63	382.5	1214.56	911.85	2401.43	1356.7	−2.3	−19.2
9	609.61	488.14	1303.6	1093.96	2821.81	1571.72	−3.6	−32.7
10	460.68	289.05	1117.34	999.51	2181.71	1660.25	−2.0	−25.1
11	496.88	336.92	1232.47	1119.74	2355.25	1676.03	−1.6	−35.0
12	387.86	242.09	1113.91	968.43	2094.58	1680.86	−1.6	−22.9
13	431.65	332.46	1125.18	1000.62	2277.07	1632.53	−2.5	−25.2
14	435.59	241.65	1113.46	1080.89	2529.66	1896.28	−2.6	−31.6
15	445.53	244.25	1196.34	941.42	2280.94	1512.41	−2.6	−21.1
16	480.23	393.58	1134.02	972.68	2239.45	1554.84	−2.4	−23.2
17	491.09	287	1064.44	892.09	1955	1155	−2.0	−18.0
Min	356.38	225.83	1064.44	833.24	1955	1155		
Max	618.2	496.24	1303.6	1119.74	2821.81	1896.28		

Using the Voxler[®] 4 program, a 3D velocity distribution was built up from the 2D models that were obtained by inverting the shallow refraction data in the investigated site [40]. The comparison and correlation of all the computed models highly depended on this data presentation. The P-wave and S-wave velocities along the seventeen measurement profiles are shown in the three-dimensional fence diagram (Figure 11). This figure reveals the former three interpreted geoseismic strata, which were distinguished identically based on the vertical and horizontal velocity distributions. Figure 12 displays the contour maps of the seismic P- and S-wave velocity variations along the study site for the three layers. These figures show the horizontal velocity changes due to lithological changes. They revealed that the lithology was not identical everywhere due to changes in the physical properties of soils/rocks throughout the layers. Figure 13 shows a shading color relief map of the depths to the top of the second and third layers from the seismic data. The thickness of the first layer increased to the east and west central sides of the site, decreased to the north and south, and reached a minimum value in the southeastern and northwestern parts of the site. The thickness of the second layer increased in the north and south directions and decreased in the east and west directions.

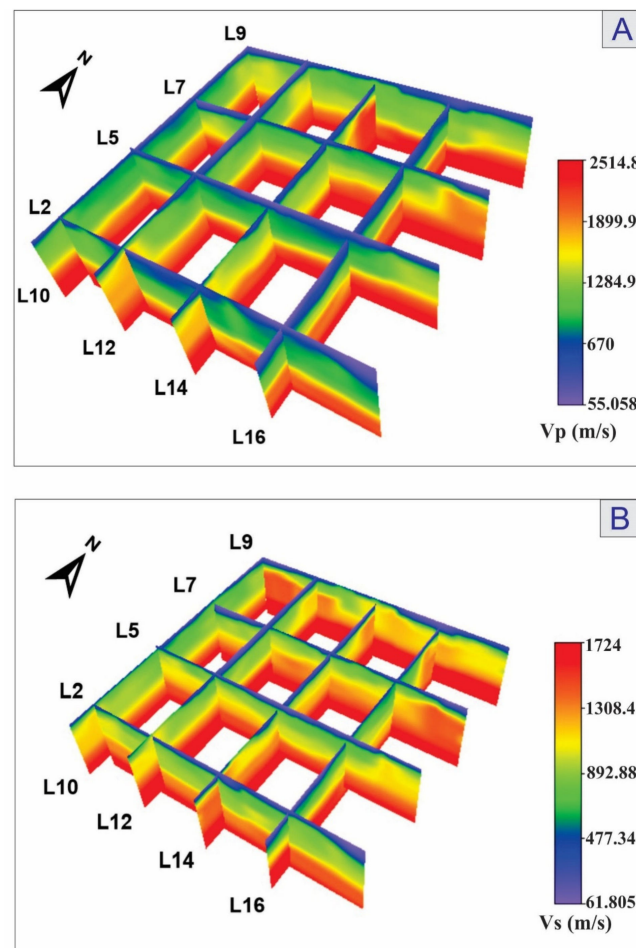


Figure 11. (A) Three-dimensional fence diagrams depicting the velocity variations for the P-wave and (B) S-wave along the surveyed profiles. The three interpreted geoseismic layers are shown in this figure. They were all differentiated using the vertical and horizontal velocity distributions.

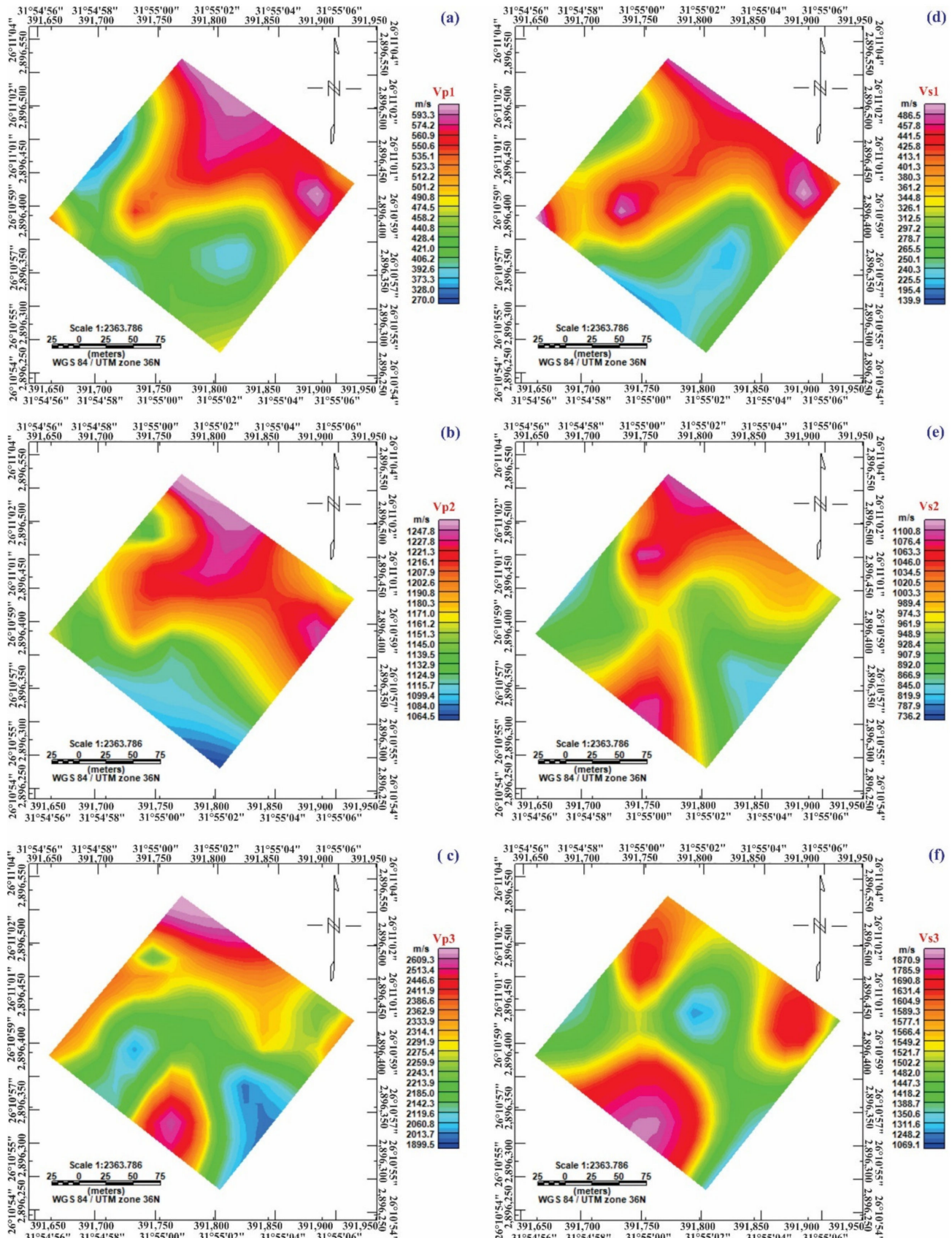


Figure 12. Zonation maps showing the spatial variation of seismic P- and S-wave velocities for three layers along the study site, as shown in the (a) V_p of the first layer, (b) V_p of the second layer, (c) V_p of the third layer, (d) V_s of the first layer, (e) V_s of the second layer, and (f) V_s of the third layer.

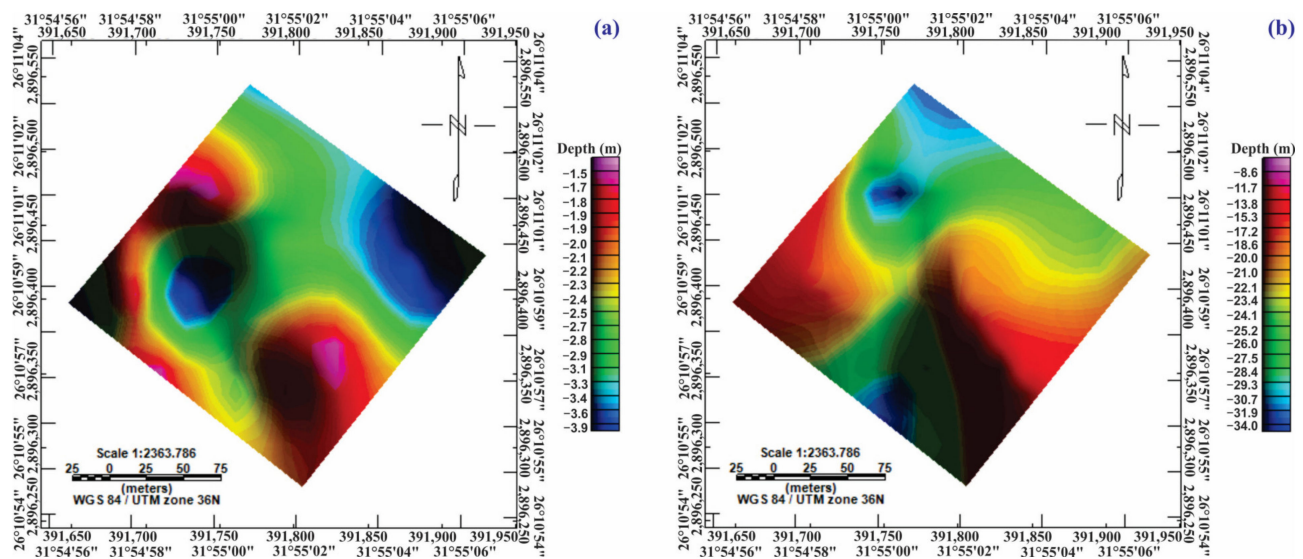


Figure 13. The depths to the top of the second (a) and third (b) layers are depicted on a shaded color relief map using the seismic results.

6. Calculation of the Elastic, Geotechnical, V_s^{30} , and Petrophysical Properties

It is necessary to describe the soil characterizations in detail utilizing several geophysical tools for the soil/rock foundation of the investigated site [33]. V_p and V_s values were utilized to estimate the elastic moduli, petrophysical properties, and geotechnical parameters of the soils/rocks of the investigated site. The calculated petrophysical parameters were the void ratio and porosity. The elastic moduli were Poisson’s ratio, the rigidity modulus, Young’s modulus, and the bulk modulus. The engineering geotechnical parameters were the materials index, concentration index, stress ratio, N-value, settlement, ultimate bearing capacity, and V_s^{30} . Table 2 summarizes all the preceding parameters, equations, and references. Table 3 contains the results of all these parameter estimations based on the V_p and V_s values.

Table 2. Explanations for the main petrophysical, elastic, and geotechnical variables that were utilized in this study.

Type	Parameter	The Formula Employed	References
Petrophysical parameters	Porosity (Φ)	$\Phi = -0.175 \ln (V_p) + 1.56$	[41]
	Void ratio (e)	$e = \Phi / (1 - \Phi)$	[42,43]
Elastic moduli and density	Rock density (ρ)	$\rho = aV_p^{0.25}$ V_p in m/s, a = 0.31 when the density is given in g/cm ³ .	[44]
	Poisson’s ratio (σ)	$\sigma = \frac{(V_p/V_s)^2 - 2}{2(V_p/V_s)^2 - 2}$	[45]
	Rigidity modulus (μ)	$\mu = \rho V_s^2$	[46]
	Young’s modulus (E)	$E = \rho V_s^2 \frac{(3V_p^2 - 4V_s^2)}{(V_p^2 - V_s^2)}$	[47]
	Bulk modulus (K)	$K = \rho (V_p^2 - \frac{3}{4} V_s^2)$	[48]

Table 2. Cont.

Type	Parameter	The Formula Employed	References
Geotechnical parameters	Concentration index (Ci)	$C_i = \left[3 - 4 \left(\frac{V_s^2}{V_p^2} \right) \right] / \left[1 - 2 \left(\frac{V_s^2}{V_p^2} \right) \right]$	[49]
	Stress Ratio (Si)	$S_i = 1 - 2 \left(\frac{V_s^2}{V_p^2} \right) = (C_i - 2)^{-1}$	[49]
	Material Index (Mi)	Mi = (1 - 4σ) where σ is Poisson’s ratio	[50]
	Liquefaction potentiality (N-value)	$V_s = 89.9 * N^{0.341}$	[51,52]
	Ultimate bearing capacity (qult)	$q_{ult} \cong \gamma V_s(0.1) = \rho V_s(\text{kN/m}^2)$ $q_{ult} = 1/100\rho V_s(\text{kg/m}^2)$ where γ is the ground’s unit weight, ρ is the density of the rocks, and V _s is the velocity of the shear waves.	[53]
V _s ³⁰	Settlement (δ)	$\delta_z = \frac{q_{ult}}{E} Z$ $Z^2 = \frac{3}{4\pi} \frac{q_{ult}}{0.333}$ where: q _{ult} for the load at unit area is the stress value depending on the depth z, δ _z is the settlement value for the soil column with the depth z.	[54]
	V _s ³⁰	$V_{s30} = \frac{30}{\sum_{i=1}^N \left(\frac{d_i}{V_{s_i}} \right)}$ where Vi and hi indicate the thickness (m) and the V _s of the i th layer present in the top 30 m, respectively.	[55]

6.1. Petrophysical Parameters

The following is a brief description of the petrophysical results:

The porosity values ranged between 0.44 and 0.53 for the first layer, between 0.31 and 0.34 for the second one, and between 0.18 and 0.23 for the third one. The porosity values of the first layer were relatively high, which was attributed to incompetent and variable soil/rock associated with wadi deposits. The second layer’s porosity was distinguished by an intermediate porosity that reflected the sand and muddy sand layers. The clay deposits were revealed by the porosity of the third layer, which was composed of low-porosity materials.

The void ratios were between 0.77 and 1.14 for the first layer, between 0.44 and 0.52 for the second layer, and between 0.20 and 0.31 for the third layer. The third layer was characterized by a layer with a decreased void ratio that revealed competent materials.

6.2. Elastic Moduli

Table 3 summarizes the calculated elastic moduli, the petrophysical properties, and geotechnical parameters of the soils/rocks of the investigated site using V_p and V_s values for all 17 seismic profiles. The following is a summary of the elastic moduli findings:

The densities for the first, second, and third layers ranged from 1.35 to 1.55 g/cm³, 1.77 to 1.86 g/cm³, and 2.06 to 2.26 g/cm³, respectively. According to Gardner et al. [44], seismic wave velocities and density are directly related. Accordingly, the density increased with increasing seismic wave velocity, which increased the degree of soil/rock competence. The density results showed that the density gradually increased from the first to the third layer, indicating that the third layer had high density values due to the highly competent materials and greater burial depth.

Poisson’s ratio values of this site ranged from -1.29 to 0.29, -7.67 to -0.05, and -0.4 to 0.28 for the first, second, and third layers, respectively. Lowly competent rocks possessed a higher Poisson’s ratio and vice versa. The Poisson ratio findings demonstrated that the first layer was made up of less competent materials, whilst the second and third levels comprised fairly to moderately competent materials.

Table 3. The various petrophysical, elastic, V_s^{30} , and geotechnical variables in the investigated region.

P.	Layer	Petrophysical		Elastic Moduli and Density					Geotechnical Parameters					V_s^{30} (m/s)		
		Φ	e	ρ (g/cm ³)	σ	μ (dyn/cm ²)	E (dyn/cm ²)	K (dyn/cm ²)	Ci	Si	Mi	N-Value	Qult (kg/cm ²)		δ (cm)	
1	1	0.47	0.89	1.47	-1.29	2.95×10^9	1.73×10^9	1.60×10^8	0.23	-0.56	6.17	>50	3.32	-4.59×10^{-3}	1044.8	
	2	0.33	0.48	1.81	-0.30	1.48×10^{10}	2.06×10^{10}	4.29×10^9	-2.31	-0.23	2.21		26.11	2.37×10^{-2}		
	3	0.21	0.26	2.14	0.09	4.89×10^{10}	1.06×10^{11}	4.29×10^{10}	12.48	0.10	0.65		118.17	9.42×10^{-2}		
2	1	0.51	1.04	1.39	-0.55	1.52×10^9	1.36×10^9	2.16×10^8	-0.81	-0.36	3.21	45.7	1.37	9.87×10^{-4}	1162.8	
	2	0.33	0.49	1.79	-0.49	1.51×10^{10}	1.52×10^{10}	2.55×10^9	-1.02	-0.33	2.98		27.17	3.47×10^{-2}		
	3	0.21	0.27	2.13	0.12	4.68×10^{10}	1.05×10^{11}	4.52×10^{10}	9.67	0.13	0.54		110.95	8.45×10^{-2}		
3	1	0.45	0.82	1.51	-1.06	3.73×10^9	4.34×10^8	4.63×10^7	0.05	-0.51	5.23	>50	4.49	-3.34×10^{-2}	983.7	
	2	0.32	0.47	1.83	-0.16	1.50×10^{10}	2.53×10^{10}	6.39×10^9	-5.28	-0.14	1.64		26.37	1.97×10^{-2}		
	3	0.23	0.30	2.08	-0.24	5.01×10^{10}	7.65×10^{10}	1.73×10^{10}	-3.24	-0.19	1.94		127.41	1.52×10^{-1}		
4	1	0.52	1.08	1.37	0.23	6.99×10^8	1.72×10^9	1.06×10^9	5.34	0.30	0.08	14.9	0.45	8.32×10^{-5}	1235.4	
	2	0.33	0.48	1.81	-0.05	1.25×10^{10}	2.39×10^{10}	7.28×10^9	-20.32	-0.04	1.19		>50	20.53		1.26×10^{-2}
	3	0.23	0.30	2.07	-0.08	4.36×10^{10}	8.03×10^{10}	2.31×10^{10}	-11.63	-0.07	1.32		104.60	9.77×10^{-2}		
5	1	0.53	1.14	1.35	-0.18	9.88×10^8	1.61×10^9	3.92×10^8	-4.43	-0.16	1.74	25.4	0.76	2.58×10^{-4}	1115.3	
	2	0.32	0.48	1.82	-0.18	1.45×10^{10}	2.38×10^{10}	5.82×10^9	-4.54	-0.15	1.72		25.20	1.92×10^{-2}		
	3	0.20	0.25	2.16	0.20	4.43×10^{10}	1.07×10^{11}	6.00×10^{10}	5.90	0.26	0.18		100.66	6.81×10^{-2}		
6	1	0.45	0.81	1.52	-0.11	2.77×10^9	4.90×10^9	1.33×10^9	-7.76	-0.10	1.46	>50	2.89	1.22×10^{-3}	1046.5	
	2	0.32	0.46	1.83	-0.15	1.55×10^{10}	2.66×10^{10}	6.85×10^9	-5.87	-0.13	1.58		27.47	2.04×10^{-2}		
	3	0.21	0.27	2.13	0.26	3.38×10^{10}	8.53×10^{10}	5.97×10^{10}	4.81	0.36	-0.05		69.01	4.01×10^{-2}		
7	1	0.44	0.77	1.55	-0.40	3.81×10^9	4.53×10^9	8.33×10^8	-1.47	-0.29	2.62	>50	4.49	3.19×10^{-3}	899.1	
	2	0.31	0.46	1.84	-0.31	1.73×10^{10}	2.39×10^{10}	4.90×10^9	-2.21	-0.24	2.24		32.12	3.10×10^{-2}		
	3	0.21	0.27	2.13	-0.19	6.21×10^{10}	1.01×10^{11}	2.44×10^{10}	-4.32	-0.16	1.75		85.71	5.21×10^{-2}		
8	1	0.46	0.85	1.49	-0.02	2.18×10^9	4.26×10^9	1.35×10^9	-40.14	-0.02	1.10	>50	2.09	7.39×10^{-4}	1108.3	
	2	0.32	0.46	1.83	-0.15	1.52×10^{10}	2.60×10^{10}	6.70×10^9	-5.86	-0.13	1.58		26.74	1.97×10^{-2}		
	3	0.20	0.25	2.17	0.27	3.99×10^{10}	1.01×10^{11}	7.18×10^{10}	4.77	0.36	-0.06		168.00	2.01×10^{-1}		

Table 3. Cont.

P.	Layer	Petrophysical		Elastic Moduli and Density					Geotechnical Parameters					V _s ³⁰ (m/s)	
		Φ	e	ρ (g/cm ³)	σ	μ (dyn/cm ²)	E (dyn/cm ²)	K (dyn/cm ²)	Ci	Si	Mi	N-Value	Qult (kg/cm ²)		δ (cm)
9	1	0.44	0.78	1.54	−0.39	3.67 × 10 ⁹	4.45 × 10 ⁹	8.30 × 10 ⁸	−1.54	−0.28	2.57		4.28	2.95 × 10 ^{−3}	805.0
	2	0.31	0.44	1.86	−0.69	2.23 × 10 ¹⁰	1.38 × 10 ¹⁰	1.93 × 10 ⁹	−0.45	−0.41	3.76		45.60	1.08 × 10 ^{−1}	
	3	0.17	0.20	2.26	0.28	5.58 × 10 ¹⁰	1.42 × 10 ¹¹	1.05 × 10 ¹¹	4.63	0.38	−0.10		131.94	8.77 × 10 ^{−2}	
10	1	0.49	0.95	1.44	0.18	1.20 × 10 ⁹	2.82 × 10 ⁹	1.45 × 10 ⁹	6.70	0.21	0.30	30.7	0.92	2.16 × 10 ^{−4}	936.6
	2	0.33	0.50	1.79	−1.50	1.79 × 10 ¹⁰	1.80 × 10 ¹⁰	1.50 × 10 ⁹	0.33	−0.60	7.01	>50	34.99	−4.88 × 10 ^{−2}	
	3	0.22	0.27	2.12	−0.19	5.84 × 10 ¹⁰	9.48 × 10 ¹⁰	2.30 × 10 ¹⁰	−4.32	−0.16	1.75		154.93	1.82 × 10 ^{−1}	
11	1	0.47	0.90	1.46	0.07	1.66 × 10 ⁹	3.57 × 10 ⁹	1.40 × 10 ⁹	14.43	0.08	0.70	48.2	1.44	4.18 × 10 ^{−4}	833.2
	2	0.32	0.46	1.84	−1.86	2.30 × 10 ¹⁰	3.98 × 10 ¹⁰	2.80 × 10 ⁹	0.46	−0.65	8.46	>50	48.82	−4.30 × 10 ^{−2}	
	3	0.20	0.25	2.16	−0.01	6.07 × 10 ¹⁰	1.20 × 10 ¹¹	3.89 × 10 ¹⁰	−76.18	−0.01	1.05		159.29	1.52 × 10 ^{−1}	
12	1	0.52	1.07	1.38	0.18	8.06 × 10 ⁸	1.90 × 10 ⁹	9.94 × 10 ⁸	6.53	0.22	0.28	18.3	0.55	1.13 × 10 ^{−4}	991.6
	2	0.33	0.50	1.79	−1.05	1.68 × 10 ¹⁰	1.61 × 10 ⁹	1.73 × 10 ⁸	0.05	−0.51	5.19	>50	31.90	−4.53 × 10 ^{−1}	
	3	0.22	0.29	2.10	−0.40	5.93 × 10 ¹⁰	7.06 × 10 ¹⁰	1.30 × 10 ¹⁰	−1.47	−0.29	2.62		160.64	2.62 × 10 ^{−1}	
13	1	0.50	0.99	1.41	−0.23	1.56 × 10 ⁹	2.41 × 10 ⁹	5.50 × 10 ⁸	−3.36	−0.19	1.92	46.3	1.39	5.74 × 10 ^{−4}	917.3
	2	0.33	0.49	1.80	−1.39	1.80 × 10 ¹⁰	1.40 × 10 ¹⁰	1.24 × 10 ⁹	0.28	−0.58	6.56	>50	35.11	−6.29 × 10 ^{−2}	
	3	0.21	0.26	2.14	−0.03	5.71 × 10 ¹⁰	1.11 × 10 ¹¹	3.49 × 10 ¹⁰	−33.69	−0.03	1.12		147.47	1.41 × 10 ^{−1}	
14	1	0.50	0.99	1.42	0.28	8.27 × 10 ⁸	2.11 × 10 ⁹	1.58 × 10 ⁹	4.60	0.38	−0.11	18.2	0.54	1.01 × 10 ^{−4}	760.1
	2	0.33	0.50	1.79	−7.67	2.09 × 10 ¹⁰	2.79 × 10 ¹¹	5.69 × 10 ⁹	0.87	−0.88	31.69	>50	44.02	−4.98 × 10 ^{−3}	
	3	0.19	0.23	2.20	−0.14	7.91 × 10 ¹⁰	1.36 × 10 ¹¹	3.52 × 10 ¹⁰	−6.07	−0.12	1.57		228.78	2.77 × 10 ^{−1}	
15	1	0.49	0.97	1.42	0.29	8.50 × 10 ⁸	2.18 × 10 ⁹	1.69 × 10 ⁹	4.51	0.40	−0.14	18.7	0.56	1.04 × 10 ^{−4}	907.5
	2	0.32	0.47	1.82	−0.31	1.62 × 10 ¹⁰	2.22 × 10 ¹⁰	4.54 × 10 ⁹	−2.19	−0.24	2.25		29.36	2.79 × 10 ^{−2}	
	3	0.21	0.26	2.14	0.11	4.90 × 10 ¹⁰	1.09 × 10 ¹¹	4.61 × 10 ¹⁰	10.29	0.12	0.57		117.87	9.18 × 10 ^{−2}	
16	1	0.48	0.92	1.45	−0.52	2.25 × 10 ⁹	2.14 × 10 ⁹	3.49 × 10 ⁸	−0.91	−0.34	3.09	>50	2.28	1.73 × 10 ^{−3}	1001.7
	2	0.33	0.49	1.80	−0.89	1.70 × 10 ¹⁰	3.68 × 10 ⁹	4.41 × 10 ⁸	−0.12	−0.47	4.57		32.31	2.03 × 10 ^{−1}	
	3	0.21	0.27	2.13	0.03	5.16 × 10 ¹⁰	1.07 × 10 ¹¹	3.82 × 10 ¹⁰	29.85	0.04	0.86		127.83	1.10 × 10 ^{−1}	
17	1	0.48	0.91	1.46	0.24	1.20 × 10 ⁹	2.98 × 10 ⁹	1.91 × 10 ⁹	5.16	0.32	0.04	30.1	0.90	1.96 × 10 ^{−4}	1105.1
	2	0.34	0.52	1.77	−0.68	1.41 × 10 ¹⁰	9.02 × 10 ⁹	1.27 × 10 ⁹	−0.47	−0.40	3.72	>50	25.07	5.00 × 10 ^{−2}	
	3	0.23	0.31	2.06	0.23	2.75 × 10 ¹⁰	6.78 × 10 ¹⁰	4.21 × 10 ¹⁰	5.31	0.30	0.07		53.47	3.03 × 10 ^{−2}	

The rigidity moduli for the first, second, and third layers ranged from 6.99×10^8 to 3.81×10^9 , 1.25×10^{10} to 2.30×10^{10} , and 2.75×10^{10} to 7.91×10^{10} dyn/cm², respectively. It was concluded that the third layer was compacted clay based on the considerably large rigidity modulus values.

The Young's moduli of the first, second, and third layers ranged from 4.34×10^8 to 4.90×10^9 , 1.61×10^9 to 2.79×10^{11} , and 6.78×10^{10} to 1.42×10^{11} dyn/cm², respectively. The third layer was distinguished by comparatively high values. The high Young's modulus values indicated that the material was inelastic or stiff.

The bulk moduli (k) of the first, second, and third layers were, respectively, 4.63×10^7 to 1.91×10^9 , 1.73×10^8 to 7.28×10^9 , and 1.30×10^{10} to 1.05×10^{11} dyn/cm². The third layer was distinguished by comparatively high values. Low bulk modulus substances are compressible and vice versa.

6.3. Geotechnical Parameters

The following is a compilation of the geotechnical parameter results for the designated layers:

The concentration indexes for the first, second, and third layers ranged from -40.14 to 14.43 , -20.32 to 0.87 , and -76.18 to 29.85 , respectively. Abd El-Rahman [50] asserted that concentration index values are greater in the more competent (third layer) materials and lower in the soft ones (first layer).

The stress indexes for the first, second, and third layers ranged from -0.56 to 0.4 , -0.88 to -0.04 , and -0.29 to 0.38 , respectively. It will be greater for loose, cohesionless soils (first layer), hence a higher stress ratio indicates that the rock is less compact [50].

The material indexes for the first, second, and third layers were -0.14 to 6.17 , 1.19 to 31.69 , and -0.1 to 2.62 , respectively. The material index values for foundation applications are classified into four major groups [56,57]. The first, second, and third layers were related to the materials in category I of incompetent to slightly competent materials, category II of fairly to moderately competent, and category IV of very highly competent materials, respectively.

The standard penetration test (SPT) results, or the N-values, for the first layer were 14.9 in some profiles and >50 in other profiles, whereas the N-values were >50 for the second and third layers. According to [56,57], the higher the N-value, the harder it is for the rock to be pierced, and thus, the greater the degree of competence. In contrast to the second and third layers, which were characterized by dense to extremely dense materials, the first layer had low N-values due to the abundance of weathered materials and decreasing compaction of these particles.

The ultimate bearing capacities (qult) for the first, second, and third layers ranged from 0.45 to 4.49 , 20.53 to 48.82 , and 53.47 to 228.78 kg/cm², respectively. The third layer had the highest values, reflecting competent materials, while the uppermost layer had the lowest values of competent soils.

The settlement (δ) values for the first, second, and third layers ranged from -3.34×10^{-2} to 3.19×10^{-3} , -4.53×10^{-1} to 2.03×10^{-1} , and 3.03×10^{-2} to 2.77×10^{-1} cm, respectively. When soil shear stresses exceed the soil's shear strength, it is regarded as a foundation failure.

6.4. V_s^{30} of Soil and Rocks

For near-surface geologic units, V_s^{30} (average V_s for the highest 30 m) was determined using NEHRP's guidelines [7]. The suggested location was categorized as site class B (rocks) for all locations of the surveyed profiles ($760 \text{ m/s} \leq V_s^{30} < 1500 \text{ m/s}$). As crucial inputs for building design, these factors were primarily utilized.

Finally, the integration of petrophysical and geotechnical parameters and the elastic moduli revealed that the third layer was composed of competent clays, which were characterized by low values of the porosity, the void ratio, Poisson's ratio, and the stress ratio. It also had a high rigidity, Young's and bulk moduli, high concentration and material indexes,

N-value, ultimate bearing capacities, and density values, and vice versa for the first layer. When construction activities begin, the information about the degree of competence for the identified layers derived from the geotechnical parameters should be taken into account.

7. Conclusions

To investigate the features of various shallow subsurface layers, seismic refraction tomography for P- and S-wave measurements was used. The main important strategic objectives of this research were to calculate the geotechnical properties, elastic moduli, degree of competence, and petrophysical characteristics of the soils/rocks in this significant archaeological site in addition to inferring the subsurface lithology. Seventeen shallow seismic refraction profiles were implemented at the studied site. The main results of this work revealed the following:

1. Three geoseismic layers were deduced according to the vertical and the horizontal variation in the velocities for both P- and S-waves. The lithologies of these three layers from the top to the base were (i) wadi deposits, which were made up of a mixture of gravel, sand, and silt that were distinguished by incompetent to slightly competent materials, a relatively high porosity ratio, and a larger portion of voids; (ii) sand and muddy sand deposits of reasonably to moderately competent rock quality, intermediate porosity, and greater competence than the top layer; and (iii) clay deposits of competent materials, lower void ratio, and porosity materials.
2. The thicknesses of the two successive near-surface layers varied between 1.5 and 4.8 m for the first layer and 14.7 to 35 m for the second one.
3. The site was categorized as a “B” site class according to NEHRP classification.
4. According to the interpretation of seismic wave velocities and the final geoseismic models, there was no fracturing or faulting in front of the Osirion site.

This study recommends that all the deduced factors primarily serve as important inputs for all future facilities and have an impact on the seismic risk estimation, structural design, and ranking of the site competency for development and investment purposes at the site.

Author Contributions: Conceptualization, A.M.A. and G.Z.A.A.; methodology, N.F.A., A.M.A.G. and M.A.M.; software, N.F.A., A.M.A.G. and M.A.M.; validation, A.M.A., G.Z.A.A. and M.A.M.; formal analysis, N.F.A. and M.A.M.; investigation, A.M.A.G. and M.A.M.; data curation, N.F.A. and A.M.A.G.; writing—original draft preparation, N.F.A., A.M.A.G. and M.A.M.; writing—review and editing, N.F.A., A.M.A.G. and G.Z.A.A.; visualization, A.M.A.G. and M.A.M. All authors have read and agreed to the published version of the manuscript.

Funding: This research was funded by the Science, Technology, and Innovation Funding Authority (STIFA) of Egypt, grant number 37087.

Data Availability Statement: The data is available upon request from the authors.

Acknowledgments: The authors are thankful to the Science, Technology, and Innovation Funding Authority (STIFA), Egypt, for funding this work (ID number: 37087).

Conflicts of Interest: The authors declare no conflict of interest.

Abbreviations

SRT	Seismic refraction tomography
Φ	Porosity
e	Void ratio
ρ	Density
σ	Poisson’s ratio
μ	Rigidity or Shear modulus
E	Young’s modulus
K	Bulk modulus
Ci	Concentration index

Si	Stress ratio
Mi	Material index
N-value	Liquefaction Potentiality
SPT	Standard penetration test
qult	Ultimate Bearing Capacity
δ	Settlement
V_s^{30}	Averaging V_s for the highest 30 m
NEHRP	National Earthquake Hazards Reduction Program
1D	One dimension
2D	Two dimension
3D	Three dimension
T-D curve	Time Distance curve
Hz	Hertz

References

- Gaffney, C. Detecting trends in the prediction of the buried past: A review of geophysical techniques in archaeology. *Archaeometry* **2008**, *50*, 313–336. [[CrossRef](#)]
- Hasan, M.; Shang, Y.; Yi, X.; Shao, P.; He, M. Determination of rock mass integrity coefficient using a non-invasive geophysical approach. *J. Rock Mech. Geotech. Eng.* **2022**; *in press*. [[CrossRef](#)]
- Cheong, S.; Kim, Y.-J.; Chun, J.-H.; Kim, J.-K.; Huh, S. Integrated Offshore Seismic Survey Using an Unmanned Wave Glider. *Energies* **2021**, *14*, 297. [[CrossRef](#)]
- Wang, C.; Xiao, J.; Liu, W.; Ma, Z. Unloading and reloading stress-strain relationship of recycled aggregate concrete reinforced with steel/polypropylene fibers under uniaxial low-cycle loadings. *Cem. Concr. Compos.* **2022**, *131*, 104597. [[CrossRef](#)]
- Scislo, L. High Activity Earthquake Swarm Event Monitoring and Impact Analysis on Underground High Energy Physics Research Facilities. *Energies* **2022**, *15*, 3705. [[CrossRef](#)]
- Abdel Gowad, A.M.; Punzo, M.; Fiore, V.D.; Tarallo, D.; El-Haddad, A.; Al-Akraby, A.H. Shallow seismic refraction tomography and MASW survey for investigating the fractures along Qena-Safaga Road, South of Egypt. In *Engineering Geology and Geological Engineering for Sustainable Use of the Earth's Resources, Urbanization and Infrastructure Protection from Geohazards: Proceedings of the 1st GeoMEast International Congress and Exhibition, Egypt 2017 on Sustainable Civil Infrastructures 1*; Springer: Cham, Switzerland, 2017; pp. 165–191.
- NEHRP. Recommended provisions for seismic regulations for new buildings and other structures. In *Building Seismic Safety Council (BSSC) for the Federal Emergency Management Agency (FEMA 450)*; Part 1: Provisions; FEMA: Washington, DC, USA, 2003.
- BSSC (Building Seismic Safety Council). NEHRP recommended provisions for seismic regulations for new buildings and other structures. In *Report FEMA-450 (Provisions)*; Federal Emergency Management Agency (FEMA): Washington, DC, USA, 2003.
- Dobry, R.; Borchardt, R.; Crouse, C.; Idriss, I.; Joyner, W.; Martin, G.R.; Power, M.; Rinne, E.; Seed, R. New site coefficients and site classification system used in recent building seismic code provisions. *Earthq. Spectra* **2000**, *16*, 41–67. [[CrossRef](#)]
- Omer, A.; Issawi, B. Lithostratigraphical, mineralogical and geochemical studies on the Neogene and Quaternary Nile basin deposits, Qena-Assiut stretch, Egypt. In Proceedings of the 4th International Conference on Geology of the Arab World, Cairo, Egypt, 31 March 1998.
- Mahran, T.; El Haddad, A. Facies and depositional environments of Upper Pliocene-Pleistocene Nile sediments around Sohag area, Nile Valley. *J. Saharian Stud.* **1992**, *1*, 11–40.
- Brooks, J.E.; Issawi, B. *Groundwater in the Abydos Areas, Egypt; The Flooding of the Osireion*; Water Paper, Egyptian Journal of Archaeological and Restoration Studies “EJARS”: Cairo, Egypt, 1992.
- Omer, A.; Abdel Moneim, A. Geochemical characteristics of the Pliocene and Pleistocene Nile basin deposits and their influence on the groundwater chemistry in Sohag area. *Ann. Geol. Surv. Egypt* **2001**, *24*, 567–584.
- Abdel Moneim, A. Groundwater studies in and around Abydos Temples, Upper Egypt. *J. Geol. Surv. Egypt* **1999**, *22*, 357–368.
- Said, R. *The Geological Evolution of the River Nile*; Springer: New York, NY, USA, 1981; 151p.
- El-Haddad, A.; Abdel Moneim, A.; Omer, A. Influence of the transverse channels on the geometrical and hydrochemical characteristics of the Quaternary aquifer in the peripheral areas of the Nile Basin, Sohag, Egypt. In Proceedings of the Bull. of the Third International Conference on the Geology of Africa, Assuit University, Assuit, Egypt, 8–10 February 2003.
- Abdel Kareem, H. Geology of the Area West of the Nile Valley between Sohag and Girga. Master's Thesis, Assiut University, Assiut Governorate, Egypt, 1972.
- Omer, A. Geological, Mineralogical and Geochemical Studies on the Neogene and Quaternary Nile Basin Deposits, Qena-Assiut Stretch, Egypt. Ph.D. Thesis, South Valley University, Sohag, Egypt, 1996.
- Farfour, M.; Economou, N.; Abdalla, O.; Al-Taj, M. Integration of Geophysical Methods for Doline Hazard Assessment: A Case Study from Northern Oman. *Geosciences* **2022**, *12*, 243. [[CrossRef](#)]
- Farfour, M.; Al-Hosni, T. Mapping of near-surface formations by refraction seismic tomography: A case study from Al-Amerat, Sultanate of Oman. *Arab. J. Geosci.* **2020**, *13*, 1–9. [[CrossRef](#)]
- Reynolds, J.M. *An Introduction to Applied and Environmental Geophysics*, 2nd ed.; John Wiley & Sons: Hoboken, NJ, USA, 2011.

22. Dawood, A.; Akiti, T.; Glover, E. Seismic Refraction Investigation at a Radioactive Waste Disposal Site. *Geosciences* **2012**, *2*, 7–13.
23. Leucci, G.; Greco, F.; De Giorgi, L.; Mauceri, R. Three-dimensional image of seismic refraction tomography and electrical resistivity tomography survey in the castle of Occhiola (Sicily, Italy). *J. Archaeol. Sci.* **2007**, *34*, 233–242. [[CrossRef](#)]
24. Adewoyin, O.; Joshua, E.; Akinyemi, M.; Omeje, M.; Adagunodo, T.; Joel, E. Engineering Site Investigations using Surface Seismic Refraction Technique. In *IOP Conference Series: Earth and Environmental Science*; IOP Publishing: Bristol, UK, 2021; p. 012098.
25. Saad, A.; Shebl, S.; Elsamei, S.; Hamed, D. Application of Shallow Seismic Refraction To Detect Engineering Problems, Madinaty City, Egypt. *Curr. Sci. Int.* **2013**, *2*, 15–29.
26. Bery, A.A. High resolution in seismic refraction tomography for environmental study. *Int. J. Geosci.* **2013**, *4*, 792–796. [[CrossRef](#)]
27. Hunter, J.A.; Crow, H.L.; Stephenson, W.J.; Pugin, A.J.-M.; Williams, R.A.; Harris, J.B.; Odum, J.K.; Woolery, E.W. Seismic site characterization with shear wave (SH) reflection and refraction methods. *J. Seismol.* **2022**, *26*, 631–652. [[CrossRef](#)]
28. Mohammed, M.; Abudeif, A.; Abd El-aal, A. Engineering geotechnical evaluation of soil for foundation purposes using shallow seismic refraction and MASW in 15th Mayo, Egypt. *J. Afr. Earth Sci.* **2020**, *162*, 103721. [[CrossRef](#)]
29. Abudeif, A.; Mohammed, M.; Abd El-Aal, A.; Omar, K.A. Single and multi-channel passive source methods for calculating the shallow S-wave velocity structure and site effect parameters at 15th May City, Egypt. *J. Afr. Earth Sci.* **2019**, *159*, 103579. [[CrossRef](#)]
30. Kamal, H.; Saudi, G.; Abd Aal, A.A. Geological, Geotechnical and Geophysical Aspects of Zafarana Wind Farms Sites and Their Expansion at Gabel El Zeit Sites Egypt. In *IOP Conference Series: Materials Science and Engineering*; IOP Publishing: Bristol, UK, 2020; p. 012005.
31. Uhlemann, S.; Hagedorn, S.; Dashwood, B.; Maurer, H.; Gunn, D.; Dijkstra, T.; Chambers, J. Landslide characterization using P-and S-wave seismic refraction tomography—The importance of elastic moduli. *J. Appl. Geophys.* **2016**, *134*, 64–76. [[CrossRef](#)]
32. Khalil, M.H.; Hanafy, S.M. Geotechnical Parameters from Seismic Measurements: Two Field Examples from Egypt and Saudi Arabia Khalil and Hanafy: Geotechnical Parameters from Seismic Measurements. *J. Environ. Eng. Geophys.* **2016**, *21*, 13–28. [[CrossRef](#)]
33. Luna, R.; Jadi, H. Determination of dynamic soil properties using geophysical methods. In Proceedings of the First International Conference on the Application of Geophysical and NDT Methodologies to Transportation Facilities and Infrastructure, St. Louis, MO, USA, 11–15 December 2000; pp. 1–15.
34. Lehmann, B. *Seismic Traveltime Tomography for Engineering and Exploration Applications*; EAGE Publications: Houten, The Netherlands, 2007; 126p.
35. Abudeif, A.M.; Abdel Aal, G.Z.; Masoud, A.M.; Mohammed, M.A. Detection of Groundwater Pathways to Monitor Their Level Rise in Osirion at Abydos Archaeological Site for Reducing Deterioration Hazards, Sohag, Egypt Using Electrical Resistivity Tomography Technique. *Appl. Sci.* **2022**, *12*, 10417. [[CrossRef](#)]
36. Rühl, T. Determination of shallow refractor properties by 3D-CMP refraction seismic techniques. *First Break* **1995**, *13*, 69–77. [[CrossRef](#)]
37. Gebrande, H.; Miller, H. Refraktionsseismik. In *Angewandte Geowissenschaften II, Methoden der Angewandten Geophysik und Mathematische Verfahren in Geowissenschaften*; Bender, F., Ed.; Enke Verlag: Stuttgart, Germany, 1985; pp. 226–260.
38. Piip, V. Inversion of Refraction Traveltimes by Homogeneous Function Method Is Analogue of CDP Reflection Method. In Proceedings of the 71st EAGE Conference and Exhibition Incorporating SPE EUROPEC, Amsterdam, The Netherlands, 8–11 June 2009; p. cp-127-00204.
39. Leung, T. Evaluation of seismic refraction interpretation using first arrival raytracing. *Geol. Soc. Lond. Eng. Geol. Spec. Publ.* **1997**, *12*, 413–416. [[CrossRef](#)]
40. Golden Software Inc. *Surfer for Windows, Powerful Contouring and Gridding, and 3-D Surfer Mapping*; Golden Software: Golden, CO, USA, 2015.
41. Watkins, J.S.; Walters, L.A.; Godson, R.H. Dependence of in-situ compressional-wave velocity on porosity in unsaturated rocks. *Geophysics* **1972**, *37*, 29–35. [[CrossRef](#)]
42. El Sharawy, M.S.; Nabawy, B.S. Determination of electrofacies using wireline logs based on multivariate statistical analysis for the Kareem Formation, Gulf of Suez, Egypt. *Environ. Earth Sci.* **2016**, *75*, 1394. [[CrossRef](#)]
43. Nabawy, B.S.; El Sharawy, M.S. Hydrocarbon potential, structural setting and depositional environments of Hammam Faraun Member of the Belayim Formation, Southern Gulf of Suez, Egypt. *J. Afr. Earth Sci.* **2015**, *112*, 93–110. [[CrossRef](#)]
44. Gardner, G.; Gardner, L.; Gregory, A. Formation velocity and density—The diagnostic basics for stratigraphic traps. *Geophysics* **1974**, *39*, 770–780. [[CrossRef](#)]
45. Telford, W.; Geldart, L.; Sheriff, R.; Keys, D. *Applied Geophysics*; Cambridge University Press: New York, NY, USA, 1976; pp. 1–860.
46. Toksöz, M.N.; Cheng, C.; Timur, A. Velocities of seismic waves in porous rocks. *Geophysics* **1976**, *41*, 621–645. [[CrossRef](#)]
47. Othman, A.A. Construed geotechnical characteristics of foundation beds by seismic measurements. *J. Geophys. Eng.* **2005**, *2*, 126–138. [[CrossRef](#)]
48. Mott, P.H.; Dorgan, J.R.; Roland, C. The bulk modulus and Poisson’s ratio of “incompressible” materials. *J. Sound Vib.* **2008**, *312*, 572–575. [[CrossRef](#)]
49. Abd El-Rahman, M. The potential of absorption coefficient and seismic quality factor in delineating less sound foundation materials in Jabal Shib Az Sahara area, Northwest of Sanaa, Yemen Arab Republic. *Egypt MERC Earth Sci* **1991**, *5*, 181–187.
50. Abd El-Rahman, M. Evaluation of the Kinetic Moduli of the surface material and application to engineering geologic map at Ma’ Barr Sabah area (Dhamar province), Northern Yemen, Egypt. *J. Geol.* **1989**, *33*, 229–250.

51. Stümpel, H.; Kähler, S.; Meissner, R.; Milkereit, B. The use of seismic shear waves and compressional waves for lithological problems of shallow sediments. *Geophys. Prospect.* **1984**, *32*, 662–675. [[CrossRef](#)]
52. Imai, T.; Fumoto, H.; Yokota, K. *P-and S-Wave Velocities in Subsurface Layers of Ground in Japan*; Urawa Research Inst., Oyo Corporation: Saitama, Japan, 1976.
53. Keceli, A. Soil parameters which can be determined with seismic velocities. *Jeofizik* **2012**, *16*, 17–29.
54. Terzaghi, K.; Peck, R.B.; Mesri, G. *Soil Mechanics in Engineering Practice*; John Wiley & Sons: Hoboken, NJ, USA, 1996.
55. *EN 1998-1: 2004*; Eurocode 8: Design of Structures for Earthquake Resistance-Part 1: General Rules, Seismic Actions and Rules for Buildings. European Committee for Standardization: Brussels, Belgium, 2004.
56. Sheriff, R.E.; Geldart, L.P. *Exploration Seismology*; Cambridge University Press: Cambridge, UK, 1995; Volume 316.
57. Bowles, J.E. *Foundation Analysis and Design*, 2nd ed.; McGraw-Hill International Book Company: London, UK, 1988; p. 587.

Disclaimer/Publisher’s Note: The statements, opinions and data contained in all publications are solely those of the individual author(s) and contributor(s) and not of MDPI and/or the editor(s). MDPI and/or the editor(s) disclaim responsibility for any injury to people or property resulting from any ideas, methods, instructions or products referred to in the content.